COMPARING MODAL AND NODAL APPROACHES OF THE HIGH ORDER DISCOUNTINUOUS GALERKIN METHOD FOR THE SOLUTION OF SOD'S SHOCK TUBE

Alberto Costa Nogueira Junior

João Lucas de Sousa Almeida

albercn@br.ibm.com

jlsa@br.ibm.com

IBM Research Brazil

Rua Tutóia, 1157, 04007-900, São Paulo - SP, Brazil

Leonardo Machado Antonio

Cláudio Alessandro de Carvalho Silva

lmantonio@fem.unicamp.br

claudio.acsilva@gmail.com

State University of Campinas

Rua Mendeleiev 200, 13083-860, Campinas - SP, Brazil

Renato Fernandes Cantão

rfcantao@gmail.com

Federal University of São Carlos

Rodovia João Leme dos Santos (SP-264), Km 110, 18052-780, Sorocaba - SP, Brazil

Abstract. *The Sod's shock tube is the most standard test problem to assess the accuracy of numerical schemes for solving the 1D Euler equations of compressible gas dynamics. It consists of a one-dimensional Riemann problem whose time evolution gives rise to three characteristics describing the propagation speed of different regions of the system: the rarefaction wave, the contact discontinuity and the shock discontinuity. The discontinuous Galerkin method is a very suitable technique to discretize such problem as it is capable to accurately represent the smooth regions of the problem's solution while capturing the typical jump discontinuities mentioned above. In this work, we compare the two well established versions of the high-order Discontinuous Galerkin Finite Element Method (DG-FEM), namely, modal and nodal approaches*

(Karniadakis & Sherwin, 2005; Hestaven & Warburton, 2008). To ensure numerical stability along time integration, we used a viscous subcell shock capturing strategy (Persson & Peraire, 2006; Klöckner et al., 2011) with two different definitions for the artificial viscosity function: (1) elementwise constant or (2) locally C^0. Numerical experiments were devised for different configurations of degrees of freedom varying the number of elements and the polynomial degree of the interpolation basis functions. The modal and nodal DG formulations ensured stability for the Sod's problem with both types of viscous shock capturing strategies, although strategy of type 2 performed much better for both discretizations. Results showed great agreement with the analytical solution provided the number of degrees of freedom was sufficient to capture the complexity of the physical phenomena.

Keywords: *high-order, discontinuous Galerkin, compressible gas dynamics, viscous shock capturing*

1 INTRODUCTION

The shock tube is a case largely studied by Sod (1978), who compared several finite difference methods applied to one-dimensional gas dynamics problem. The tube, of a finite length, segregates by the employment of thin diaphragm a gas in two different steady conditions. The test initiates with the diaphragm removal, implying to the gas regions, in distinct conditions, to dynamically interact. This interaction results into a quite interesting features of the fluid behavior through the tube domain such as contact and shock discontinuities. The problem is naturally non linear, containing discontinuities responses and has analytical solution what makes it a well suitable base for comparison and test numerical schemes.

This work proposes a comparison of two well accepted versions of high-order discontinuous Galerkin finite element (hereinafter DG-FEM), a.k.a. modal and nodal formulations, to solve 1D Euler equations of compressible gas dynamics in the context of the Sod's shock tube problem. Basically, the difference between each approach dwells on the choice of the interpolation basis function, where the 1D modal formulation uses Legendre polynomials (Karniadakis & Sherwin, 2005) and the 1D nodal one, Lagrange polynomials (Hesthaven & Warburton, 2008). In most implementations, the choice of the quadrature points distribution use to be: Gauss-Legendre (GL) or Lobatto-Gauss-Legendre (LGL) for the modal approach and exclusively LGL for the nodal form. In order to keep comparisons as close as possible, the code implementation was made on same Python framework, modifying only the inherent characteristics of each formulation; e.g. computation of stiffness and mass matrices using the appropriate quadrature points the formulation requires. As Euler equations innately develops shocks along time integration, a sub-cell shock capturing strategy based on local artificial viscosity addition was chosen to give extra stability to the numerical scheme. The numerical model covers two viscous stabilization ways which use the following definitions for the viscous functions: (1) elementwise constant or (2) locally C^0. Shock detecting algorithm was set with the same parameters for both DG formulations. The computation of numerical fluxes for the convective and viscous operators were set as the monotone Lax-Friedrichs and the Local Discontinuous Galerkin (LDG), respectively. Nonlinear physical flux terms were treated in the same way for both discretizations performing a L^2 projection of each flux on modal space with over integration to keep consistency and stability of the method. For both approaches, a five step 4^{th} order strong stability preserving Runge-Kutta explicit integrator was used to march the set of discretized ODEs in time.

In order to compare the results of both formulations, a set of numerical experiments on Sod's shock tube was carried out. The set was composed by a variable number of mesh elements and an increasing polynomial order of approximation. The numerical results were compared to the Sod's problem analytical solution. The same set of numerical experiments was carried out for the two implemented viscous dissipation schemes of sub-cell shock capturing.

2 COMPRESSIBLE GAS DYNAMICS MODEL

The compressible gas dynamics model is described by Euler equations which govern the motion of an inviscid fluid. These equations are derived from conservation laws of mass, momentum and energy and, for one-dimension, can be written as:

$$\frac{\partial \rho}{\partial t} + \frac{\partial}{\partial x}(m) = 0 \tag{1}$$

$$\frac{\partial m}{\partial t} + \frac{\partial}{\partial x}(m^2/\rho + p) = 0 \tag{2}$$

$$\frac{\partial e}{\partial t} + \frac{\partial}{\partial x}(m(e+p)/\rho) = 0 \tag{3}$$

where ρ corresponds to the gas density, $m = \rho v$ is the linear momentum, v is the fluid velocity along x-direction, p is the gas pressure, and e is the total energy of the fluid. Considering an ideal gas, the following equation of state is valid

$$p = (\gamma - 1)(e - m^2/2\rho), \tag{4}$$

where γ is the adiabatic constant (ratio of specific heats) which is greater than 1. The system can be rewritten in vector form as:

$$\frac{\partial}{\partial t}\{u\} + \frac{\partial}{\partial x}\{f\} = 0 \tag{5}$$

where the conserved variables and non linear fluxes vectors are defined as

$$\{u\} = \left\{ \begin{array}{c} \rho \\ m \\ e \end{array} \right\}, \quad \{f\} = \left\{ \begin{array}{c} m \\ m^2/\rho + p \\ m(e+p)/\rho \end{array} \right\} \tag{6}$$

In order to avoid the undesired Gibbs effects around shock regions while keeping the advantages of high order approximations of DG-FEM , it was adopted the numerical technique of artificial viscosity addition to the gas dynamics model. In this case, the Eq. 5 is modified to include diffusive term on the right hand side

$$\frac{\partial}{\partial t}\{u\} + \frac{\partial}{\partial x}\{f\} = \frac{\partial}{\partial x}\varepsilon(x)\frac{\partial}{\partial x}\{u\} \tag{7}$$

where $\varepsilon(x)$ is the artificial viscosity function. In order to recast the new second order PDE aiming at applying the DG formulation, the system is rewritten to a 1^{st} order PDE creating an auxiliary variable q, as follows

$$\begin{aligned} &\frac{\partial}{\partial t}\{u\} + \frac{\partial}{\partial x}\left(\{f\} - \sqrt{\varepsilon(x)}\{q\}\right) = 0 \\ &\{q\} = \sqrt{\varepsilon(x)}\frac{\partial}{\partial x}\{u\} \end{aligned} \tag{8}$$

3 DISCONTINUOS GALERKIN DISCRETIZATION

The problem domain Ω is split into K non-overlapping elements with sub domains $\Omega^k = [x_l^k, x_r^k]$, where x_l^k and x_r^k are the element left and right boundary x-coordinates, respectively. On each element k, the conserved and auxiliary variables, as well as the respective non linear fluxes,

can be expressed by a polynomial expansion of degree N

$$
\begin{aligned}
x \in \Omega^k : \rho_h^k(x,t) &= \sum_{j=1}^{N+1} \hat{\rho}_j^k(t)\psi_j(x) = \sum_{i=1}^{N+1} \rho_h^k(x_i^k,t) l_i^k(x) \\
q_{\rho,h}^k(x,t) &= \sum_{j=1}^{N+1} \hat{q}_{\rho,j}^k(t)\psi_j(x) = \sum_{i=1}^{N+1} q_{\rho,h}^k(x_i^k,t) l_i^k(x) \\
f_{\rho,h}^k(\rho(x,t)) &= \sum_{j=1}^{N+1} \hat{f}_{\rho,j}^k(t)\psi_j(x) = \sum_{i=1}^{N+1} f_{\rho,h}^k(x_i^k,t) l_i^k(x)
\end{aligned} \tag{9}
$$

where $\psi_j(x)$ and $l_i^k(x)$ are the Legendre and Lagrange polynomial basis, respectively. For the sake of simplicity, only the first conserved variable ρ was written above. Thus linear momentum m and total energy e will not be explicit mentioned throughout this text. The choice of the polynomial basis defines the formulation approach: (i) Legendre polynomials, $P_n(\xi)$, $\xi \in [-1,1]$ defined on the reference element $\hat{\Omega}$ where $\psi_j^k(x(\xi)) = P_n(\xi)$ and; (ii) Lagrange polynomials on the same reference element for nodal representation. The nodal approach takes the advantage of the cardinality interpolation property, which ensures that the expansion coefficients represent the physical approximate solution in each element node. In this case, most of the calculations at the reference element are made on the local $N+1$ grid points, $x_i^k \in \Omega^k$, chosen as the Lobatto-Gauss-Legendre (LGL) quadrature points. It is worth noting that the global solution $\rho(x,t)$ (as well as the other conserved variables) is assumed to be the direct sum of the K local polynomial solutions $\rho_h^k(x,t)$,

$$
\rho(x,t) \approx \rho_h(x,t) = \bigoplus_{k=1}^{K} \rho_h^k(x,t). \tag{10}
$$

Once the local approximate solutions are defined, the residual for each element Ω^k is computed as

$$
x \in \Omega^k : R_h(x,t) = \begin{cases} \dfrac{\partial}{\partial t}\rho_h + \dfrac{\partial}{\partial x}\left(f_{\rho,h}(\rho_h)) - \sqrt{\varepsilon} q_\rho\right) \\ \\ q_\rho - \sqrt{\varepsilon}\dfrac{\partial}{\partial x}\rho_h. \end{cases} \tag{11}
$$

From the Galerkin discretization technique, the residual shall be orthogonal to all test functions $\phi_j^k(x)$, which pertain to a finite dimensional vector space $V_h^k = span\{\phi_j^k(\Omega^k)\}_{j=1}^{N+1}$, which leads to

$$
\int_{\Omega^k} R_h(x,t)\phi_j^k(x)dx = 0, \quad 1 \leq j \leq N+1. \tag{12}
$$

The Galerkin method also enforces the test functions ϕ_j^k to belong to the same set of the trial functions (Karniadakis & Sherwin, 2005) which, depending on the chosen formulation: modal

or nodal, are the Legrende or the Lagrange polynomials, respectively. Integrating Eq. (12) by parts yields the weak form of Euler equations with artificial viscosity stabilization

$$\begin{aligned}
&\int_{\Omega^k}\left(\frac{\partial \rho_h}{\partial t}\phi_j^k - f_{\rho,h}^k(\rho_h^k)\frac{d\phi_j^k(x)}{dx} + \sqrt{\varepsilon}q_{\rho,h}^k(\rho_h^k)\frac{d\phi_j^k(x)}{dx}\right)dx = -\left[\phi_j^k(x)f^*\right]_{x_l^k}^{x_r^l} \\
&+\left[\phi_j^k(x)\left(\sqrt{\varepsilon q_{\rho,h}^k}\right)^*\right]_{x_l^k}^{x_r^l}, \quad 1\le j\le N+1, \\
&\int_{\Omega^k}\left(q_{\rho,h}^k(\rho_h^k)\phi_h^k + \rho_h^k\frac{d}{dx}\left(\sqrt{\varepsilon}\phi_j^k(x)\right)\right)dx = \left[\phi_j^k(x)\left(\sqrt{\varepsilon\rho_h^k}\right)^*\right]_{x_l^k}^{x_r^l}, \quad 1\le j\le N+1,
\end{aligned} \tag{13}$$

where f^*, $\left(\sqrt{\varepsilon q_{\rho,h}^k}\right)^*$ and $\left(\sqrt{\varepsilon\rho_h^k}\right)^*$ are the numerical fluxes, which are introduced to ensure stability of the global approximate solution (Hesthaven & Warburton, 2008) enforcing communication between element boundaries. In this work, the numerical flux f^* is chosen to be the monotone Lax-Friedrichs flux, which is described in details in Hesthaven & Warburton (2008) and Nogueira & Moore (2015). The other terms, $\left(\sqrt{\varepsilon q_{\rho,h}^k}\right)^*$ and $\left(\sqrt{\varepsilon\rho_h^k}\right)^*$, associated to the second order dissipative operator, are approximated by the Local Discontinuous Galerkin (LDG) flux (Cockburn & Shu, 1998). A comprehensive description of LDG numerical flux is given in Hesthaven & Warburton (2008).

Once the numerical fluxes are defined, as well as the polynomial expansions for each formulation, the weak form described in Eq. (13) can be written in the following matrix form

$$\begin{aligned}
\frac{h^k}{2}[M]\frac{d}{dt}\{\hat{\rho}\}_h^k - [S]^T\{\hat{f}\}_{\rho,h}^k + [S^{\sqrt{\varepsilon}}]^T\{\hat{q}\}_h^k = \;& -1/2[F]_l^{k+1}\left(\{\hat{f}\}_{\rho,h}^{k+1} - C\{\hat{\rho}\}_h^{k+1}\right) \\
& -1/2[F]_r^{k}\left(\{\hat{f}\}_{\rho,h}^{k} - C\{\hat{\rho}\}_h^{k}\right) \\
& +1/2[F]_r^{k-1}\left(\{\hat{f}\}_{\rho,h}^{k-1} - C\{\hat{\rho}\}_h^{k-1}\right) \\
& +1/2[F]_l^{k}\left(\{\hat{f}\}_{\rho,h}^{k} - C\{\hat{\rho}\}_h^{k}\right) \\
& +\sqrt{\varepsilon(x_r^k)}[F]_r^k\{\hat{q}\}_{\rho,h}^k \\
& -\sqrt{\varepsilon(x_r^{k-1})}[F]_r^{k-1}\{\hat{q}\}_{\rho,h}^{k-1} \\
\frac{h^k}{2}[M]\{\hat{q}\}_h^k - [\tilde{S}^{\sqrt{\varepsilon}}]^T\{\hat{\rho}\}_h^k = \;& +1/2\left(\sqrt{\varepsilon(x_l^{k+1})} + \sqrt{\varepsilon(x_r^k)}\right)[F]_l^{k+1}\{\hat{\rho}\}_h^k \\
& -1/2\left(\sqrt{\varepsilon(x_r^{k-1})} + \sqrt{\varepsilon(x_l^k)}\right)[F]_l^{k}\{\hat{\rho}\}_h^k
\end{aligned} \tag{14}$$

wherein $\{\hat{\rho}\}_h^k$ and $\{\hat{f}\}_{\rho,h}^k$ are the vectors of time dependent degrees of freedom of the conserved variables and locally computed nonlinear fluxes. For the modal approach, these vectors correspond to the expansion coefficients of the approximate local solution, whereas for nodal formulation, they can be seen as the physical approximate solution at LGL grid points. It is worth mention that the nonlinear flux vector $\{\hat{f}\}_{\rho,h}^k$ entries are locally retrieved from the approximate solution $\{\hat{\rho}\}_h^k$, at each time step, through a L^2 projection. The description of this operation if fully detailed in Nogueira & Moore (2015). The terms $[M]$, $[S]$ and $[F]$ are the local mass, stiffness and lift matrices, respectively. The last one is associated to the element boundaries and is defined as the product $\{\phi(\xi_\Lambda)\}\{\phi(\xi_\Lambda)\}^T$, where $\{\phi(\xi_\Lambda)\}$ is a vector that contains the basis

functions evaluated at reference element $\hat{\Omega}$ boundaries. The variable $h^k/2$ is the Jacobian of the affine transformation amongst the reference element $\hat{\Omega} = [-1, 1]$ and the k^{th} grid element. The constant C, originated from Lax-Friedrichs numerical flux, is defined as the maximum eigenvalue of the flux Jacobian $\partial\{f\}/\partial\{u\}$ (Hesthaven & Warburton, 2008) and is calculated for every time step. The vector $\{\hat{q}\}_h^k$ corresponds to the auxiliary variable degrees of freedom and, as well as $\{\hat{f}\}_{\rho,h}^k$, is locally computed at each time step. The matrices $[S^{\sqrt{\varepsilon}}]$ and $[\tilde{S}^{\sqrt{\varepsilon}}]$ are related to the modified stiffness, which considers the artificial viscosity function $\varepsilon(x)$ within the integrand. Regarding Eq. (14) all the matrices entries are composed by integral forms that are numerically calculated using Gauss-Legendre (modal) or Lobatto-Gauss-Legendre (nodal) quadrature points, onto the reference element $\hat{\Omega} = [-1, 1]$, and their respective weights.

In this work, for comparison purposes, two sub-cell shock capturing methods were implemented: (i) Persson & Peraire (2006) scheme, where the artificial viscosity is defined as an elementwise constant function and (ii) the method presented by Klöckner et al. (2011), which uses a C^0 function for artificial viscosity adding. For the C^0 viscosity function, after detecting troubled cells, a maximum amount of viscosity is computed for the detected element and this value is propagated to the immediate neighboring elements using linear interpolation. If the neighbor element is not a troubled cell, the viscosity function decays linearly from the maximum value to zero keeping the total viscosity adding restricted to the troubled cells and their closest neighbors. Details about the shock detection scheme are shown in Persson & Peraire (2006) and Nogueira & Moore (2015). It is worth observing that the sub-cell shock capturing method is based on the representation of the high-order solution inside each element by an orthogonal basis, in other words, a typical modal representation. Considering this, for nodal formulation, it is necessary to compute a basis transformation using a Vandermond matrix (Hesthaven & Warburton, 2008) or a forward transformation (Karniadakis & Sherwin, 2005) before starting the detection procedure. Computationally speaking, the nodal implementation with sub-cell shock capturing is cumbersome, once it requires computations in modal space as well. Another important fact related to the nodal implementation and shock capturing schemes is that the usual LGL quadrature points purposely defined on the nodal collocation points are not enough to ensure consistent integration of the modified stiffness matrices when using C^0 artificial viscosity functions which compromise the solution stability. To overcome this limitation, it is necessary to evaluate Lagrange polynomials using more quadrature points than those of the typical spectral formulations which are not coincident to the collocation points. This clearly corrupts the most important feature of the nodal spectral formulation which assumes that collocation and quadrature points are indistinguishable.

4 NUMERICAL RESULTS

The 1D Euler equations of gas dynamics were solved for a shock tube with $1\ m$ length, where the diaphragm is placed at $0.5\ m$ segregating the gas in two different steady initial conditions. At the left side of the tube $\rho_1 = 1.000\ kg/m^3$, $u_1 = 0.0\ m/s$ and $P_1 = 1\ Pa$ and, at the right side, $\rho_2 = 0.125\ kg/m^3$, $u_2 = 0.0\ m/s$ and $P_2 = 0.1\ Pa$. The diaphragm is removed at $t_0 = 0\ s$ and the transient effects are explicitly integrated until $0.2\ s$. From this initial conditions, a set of numerical experiments was run for modal and nodal formulations with an increasing number of mesh elements and growing up the polynomial order of the interpolating basis function. For the number of elements, K, the quantities were set as $100, 200$ and 400 elements doubling the mesh size at every K increment. The polynomial order N were chosen to shift from 2^{nd}, 5^{th}, 7^{th}

and 10^{th} degrees. In order to satisfy CFL condition for the most restrictive examples ($K = 400$ and $N = 10$), dt was fixed at $2.50 \times 10^{-6}s$ which corresponds to $80,000$ time steps. The time step estimation for the explicit Runge-Kutta integrator was derived from Klöckner et al. (2011)

$$\Delta t \approx \left(C\frac{N^2}{h} + \|\varepsilon\|_{L^\infty} \frac{N^4}{h^2} \right)^{-1} \tag{15}$$

where $\|\varepsilon\|_{L^\infty}$ is the maximum amount of viscosity added to the numerical solution and h is the minimum element size. To compare the two different formulations, numerical results were plotted against the analytical solution at $t = 0.2s$. Additionally, the absolute pointwise deviation (Δ) from the analytical solution was computed as follows

$$\Delta\rho(x_i) = |\rho_n(x_i) - \rho_a(x_i)|, \tag{16}$$

where the subscripts n and a stand for to the numerical and analytical solutions, respectively, and ρ represents the density at position x_i.

The solutions were displayed only for density variable as it is enough to emphasize the main features of both DG formulations. Results were presented in groups where the artificial viscosity function and the total number of elements were fixed while the numerical solutions for modal and nodal approaches varied from top to bottom according to increasing polynomial orders. Approximate solutions were plotted against the analytical solution followed by the absolute deviation graphs.

4.1 Results for elementwise constant artificial viscosity function

Figures 1, 2 and 3 shows the approximate solutions for elementwise constant viscous dissipation considering 100, 200 and 400 elements. It can be observed that for low polynomial order ($N = 2$), the numerical solutions are too much noisy due to a very coarse discretization. Such pattern also reflects on the absolute deviation $\Delta\rho$ that shows bigger discrepancies compared to the analytical solution. For the coarsest mesh, $K = 100$, some noise can be observed also for relatively higher order ($N = 5, 7$). As expected, the higher the order the lower the deviation. In these cases, the shock discontinuity is sharply represented although the contact discontinuity is quite smeared, as well as the rarefaction region. For both formulations, spikes can be noticed over the entire solutions which confirms the bad collateral effects of using elementwise constant dissipation. For the nodal approach, in the cases with 200 and 400 elements and polynomial order $N = 2$, it was necessary to multiply the maximum amount of artificial viscosity per element, ε_0 (Persson & Peraire, 2006), by $1/2$ (reducing the total amount of viscosity added) to keep stability throughout time marching. Such exceptional modification of the artificial viscosity parameter mentioned above is only expected in extreme cases of very coarse meshes or reduced polynomial order. No parameter tweaking was made for modal formulation to guarantee stable time marching.

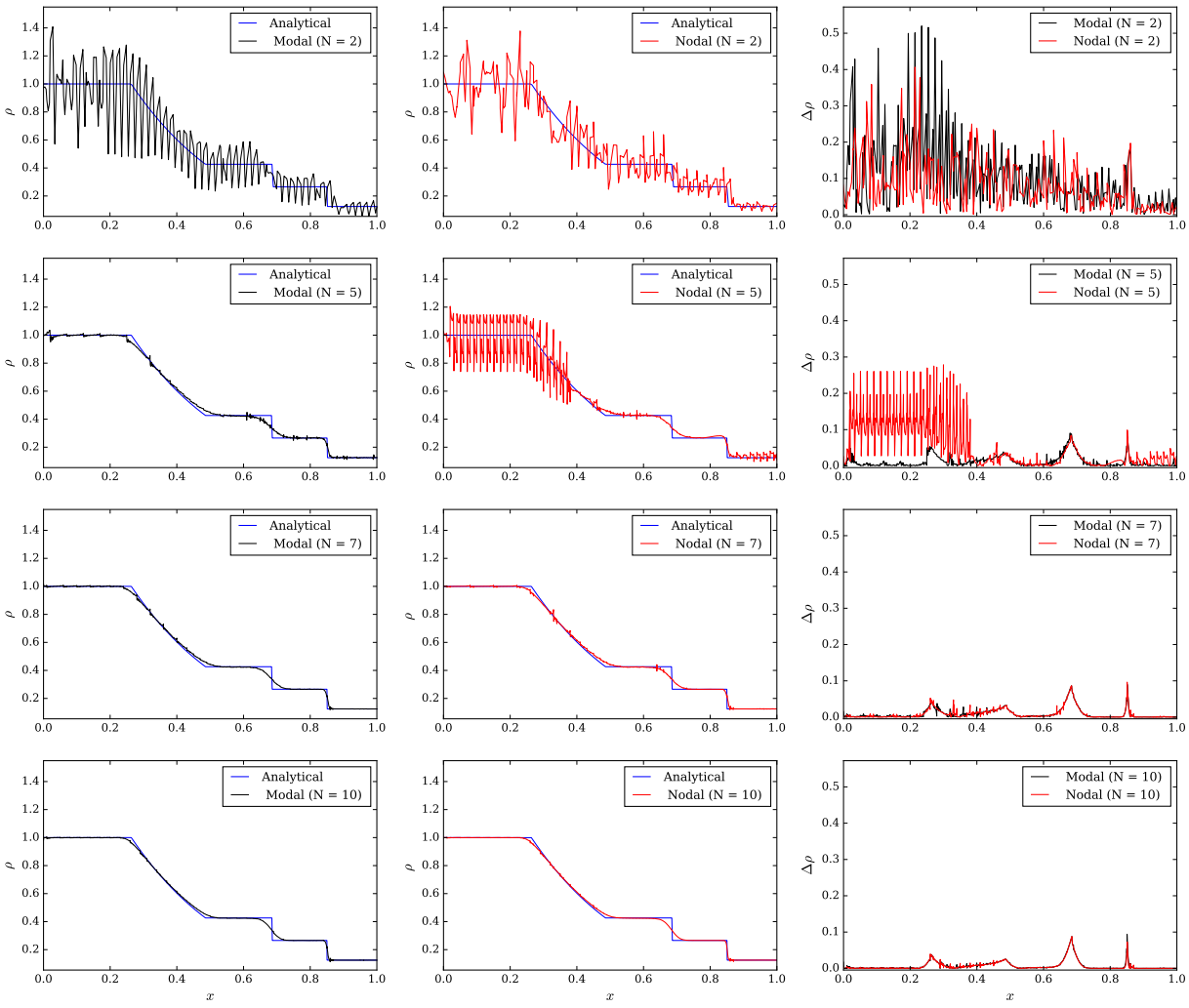

Figure 1: Density solution using 100 elements and constant artificial viscosity function

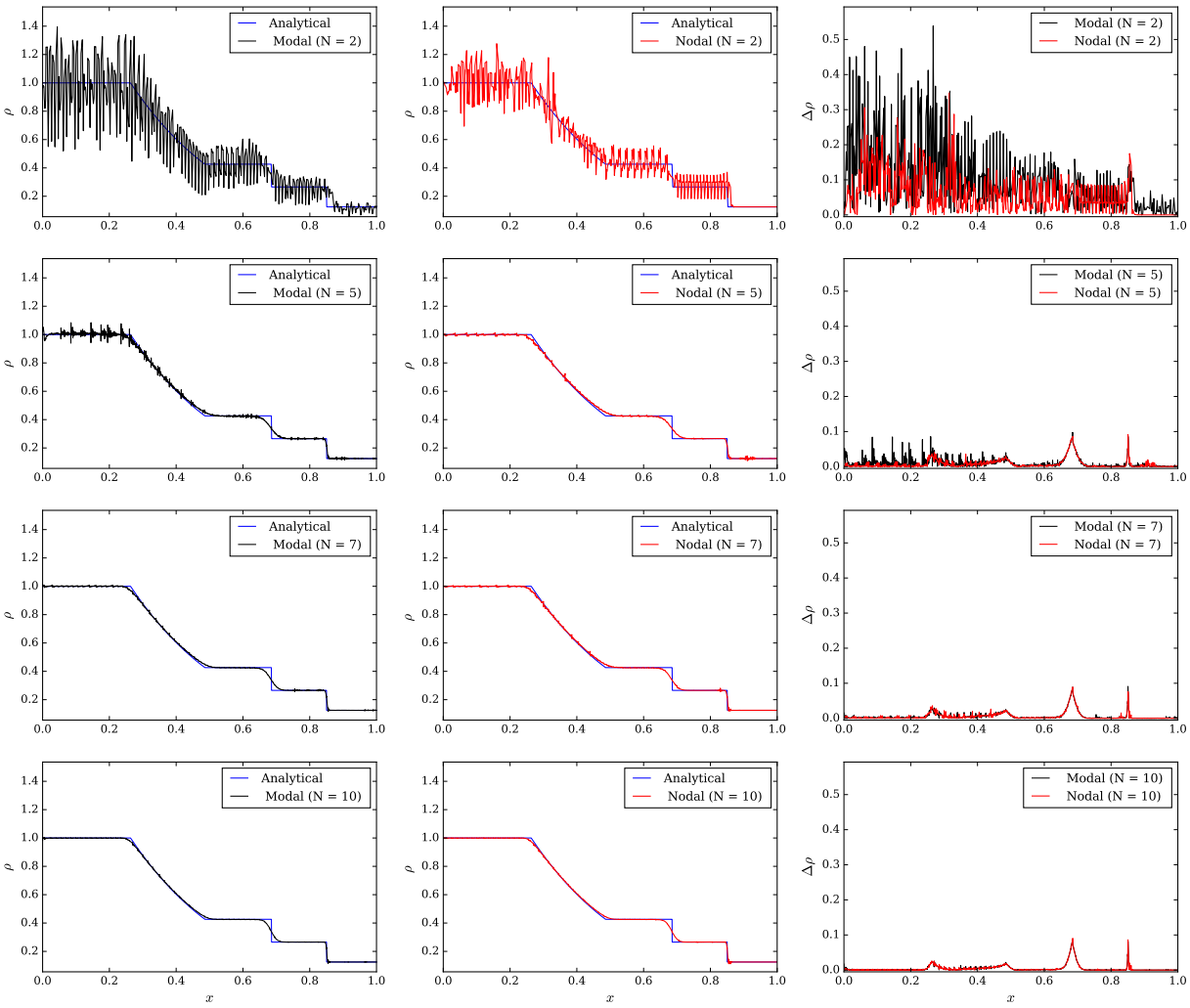

Figure 2: Density solution using 200 elements and constant artificial viscosity function.

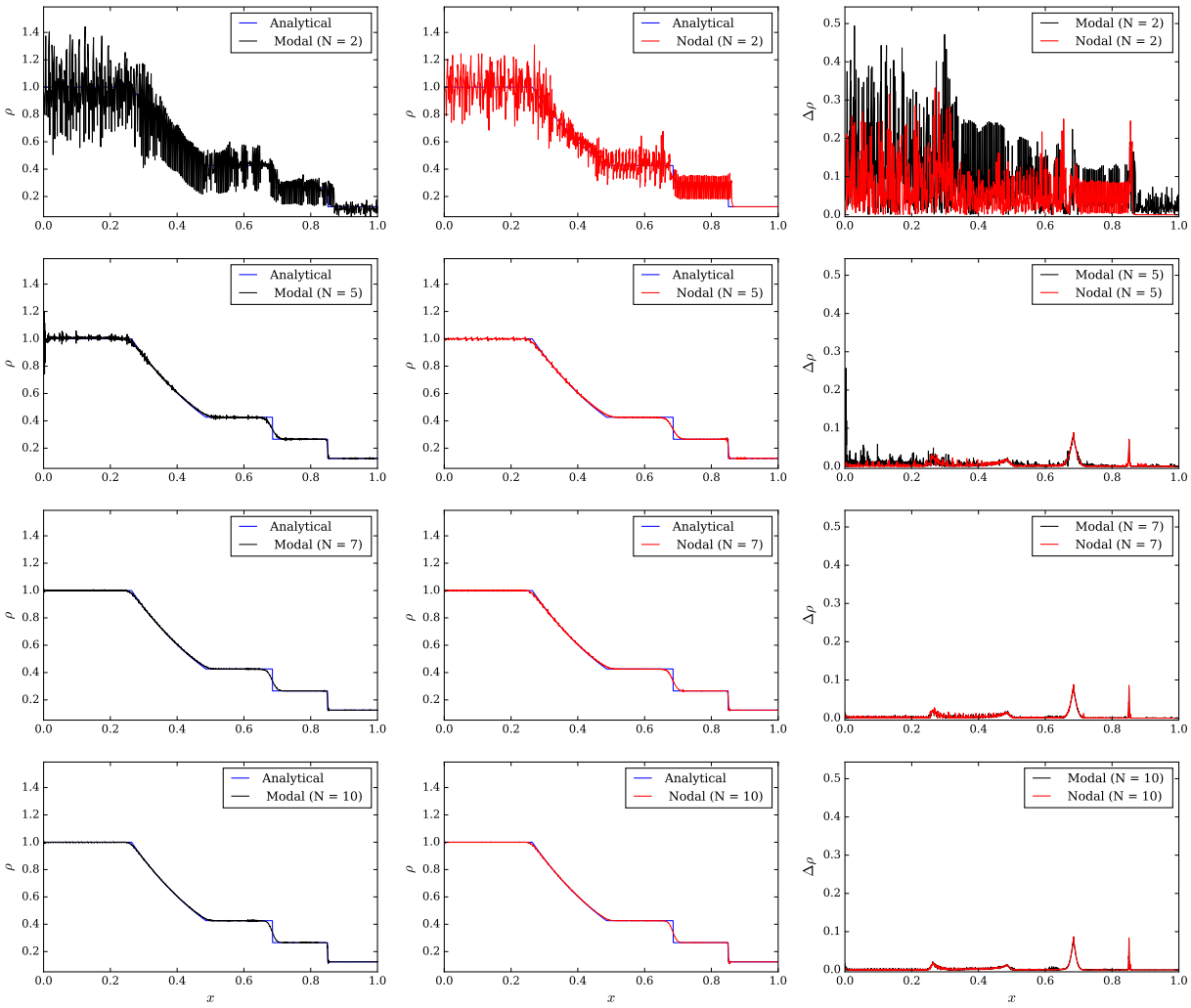

Figure 3: Density solution using 400 elements and constant artificial viscosity function.

4.2 Results for C^0 artificial viscosity function

Figures 4 and 6 show the results of the DG discretizations with C^0 viscous dissipation strategy for 100, 200 and 400 elements. From these figures, it can be observed that all approximate solutions showed very smooth response curves (no noise) for every polynomial order tested. For low order approximation ($N = 2$), the solution was smeared closer to the shock and contact discontinuities, whilst for higher order the smearing effect diminishes strongly as well as the absolute deviations. High order solutions ($N = 7, 10$) also showed very sharp shock and contact discontinuities representation. The modal formulation, for smaller polynomial orders, showed lower absolute deviations when compared to nodal DG form. In the rest of the cases, no substantial differences were observed between both formulations.

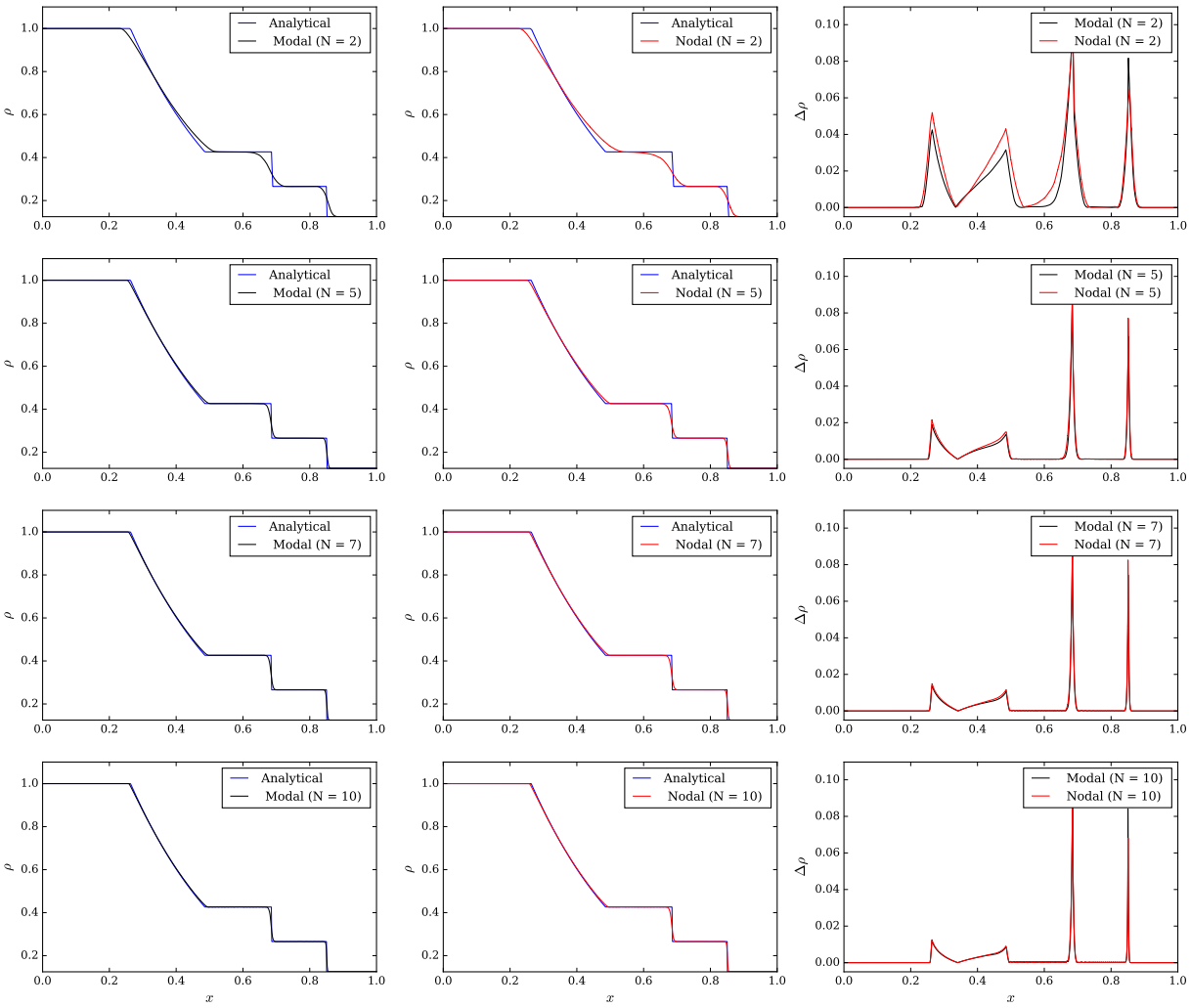

Figure 4: Density solution using 100 elements and C^0 artificial viscosity function.

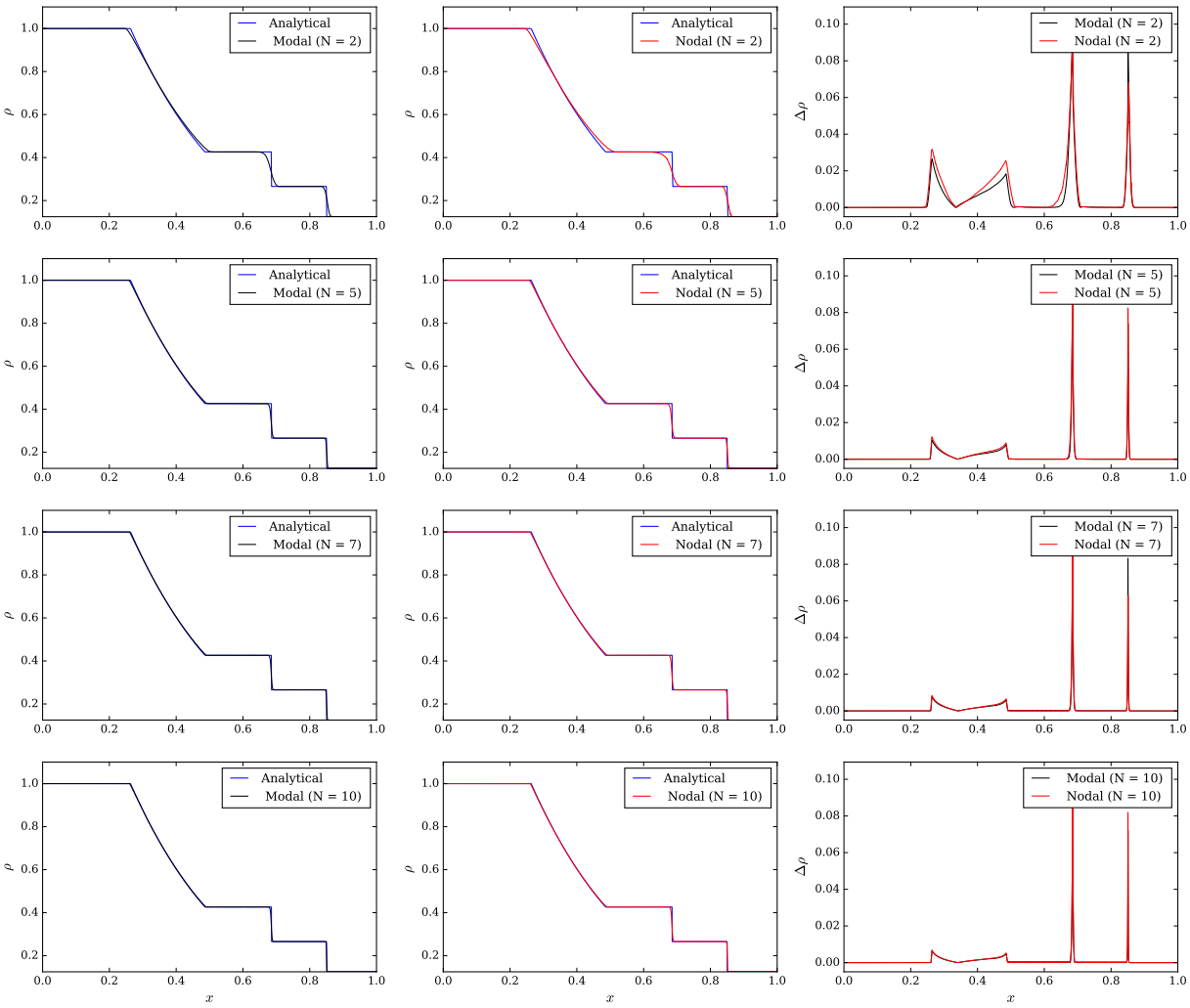

Figure 5: Density solution using 200 elements and C^0 artificial viscosity function.

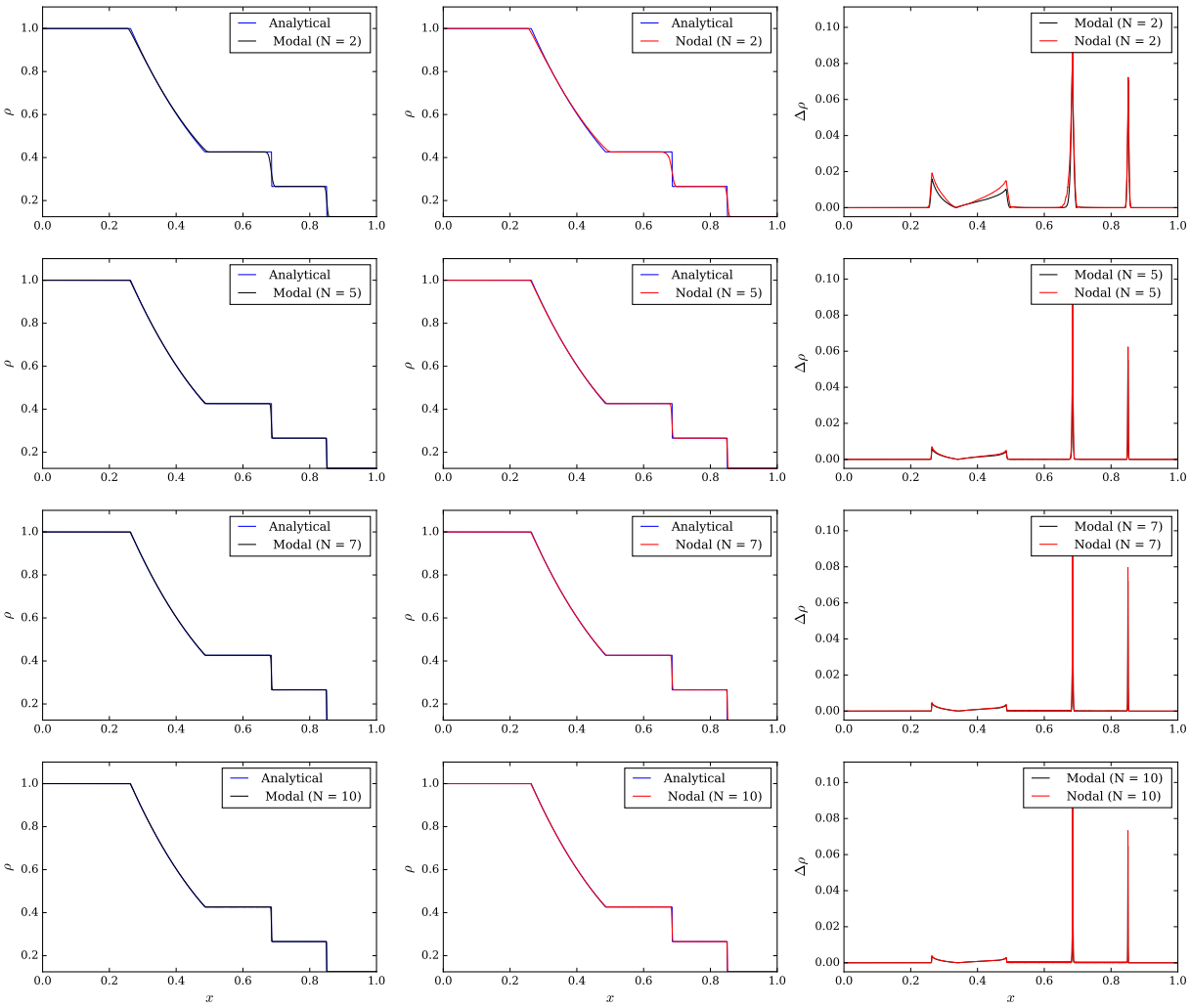

Figure 6: Density solution using 400 elements and C^0 artificial viscosity function.

4.3 Artificial viscosity distribution

Figure 7 depicts the artificial viscosity distribution inside the problem domain for all numerical experiments. Comparing both viscous dissipation strategies, it can be noticed a remarkable difference on the viscosity distributions, where, for all cases, the C^0 function kept viscous dissipation narrowly localized while the elementwise constant function spread it thoroughly the problem domain. Such results confirmed previously published works (Klöckner, et al., 2011; Nogueira, et al. 2016) that highlighted the very reliable and robust properties of the C^0 viscous function. It is worth mentioning that the higher the polynomial order of approximation the lower is the amount of artificial viscosity added. The same behavior occurs by increasing the number of elements although in a lower rate. As theoretically expected, similar behavior was observed for both DG formulations.

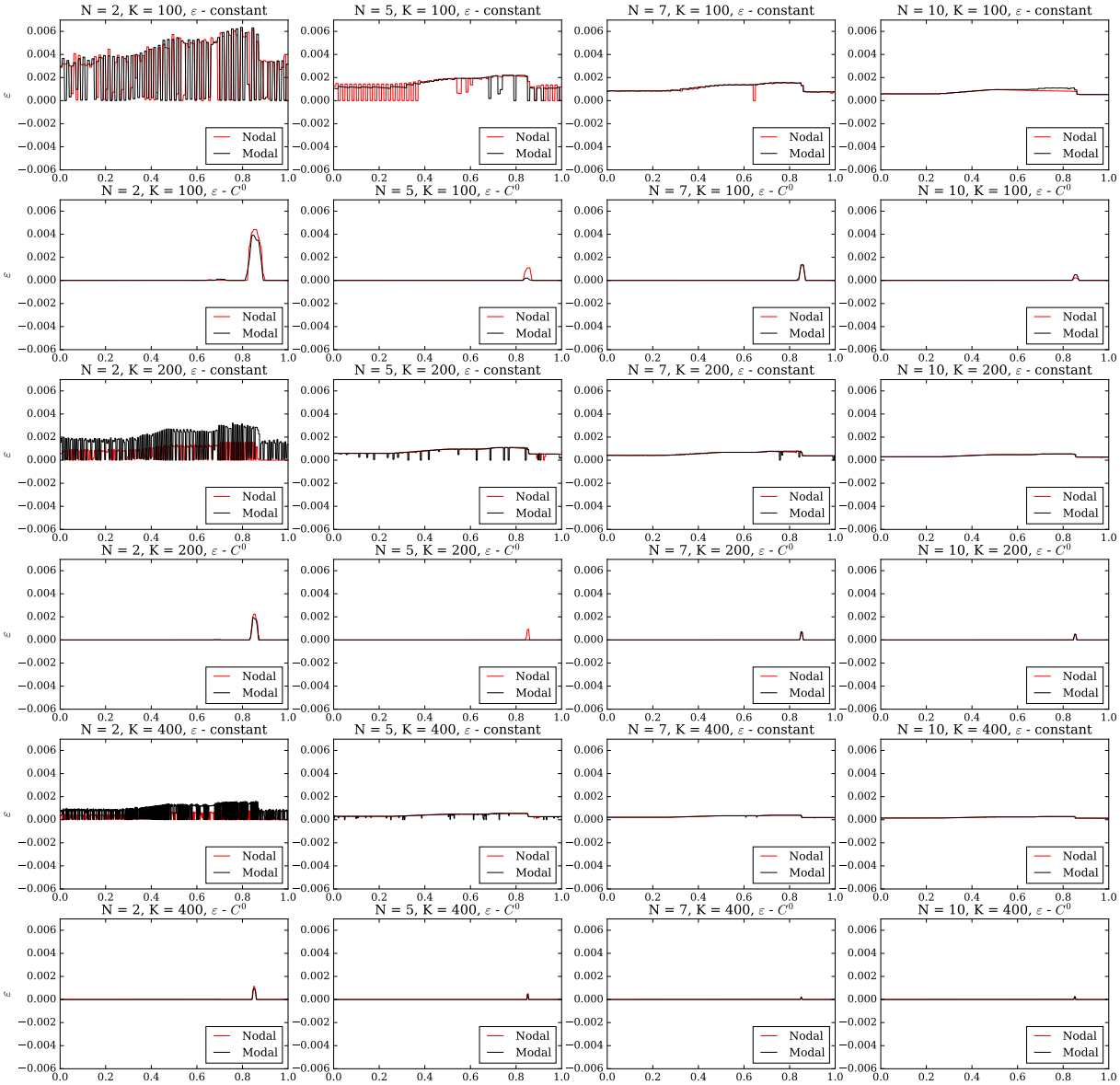

Figure 7: Artificial viscosity distribution along spatial domain.

5 CONCLUSIONS

This work compared the two standard formulations of high-order Discontinuous Galerkin, namely, modal and nodal approaches, for the 1D Euler equations of gas dynamics. The case study considered was the Sod's shock tube initial condition stabilized by two different sub-cell shock capturing schemes. Comparisons were made from a comprehensive set of numerical experiments and, apart from some pathological cases where very coarse meshes or very low polynomial order of approximation were used, both schemes showed mathematically equivalent as theoretically anticipated in Karniadakis & Sherwin (2005). However, from the computational point of view, the two approaches revealed some important differences. The nodal formulation demonstrated more computationally intensive due to the nonlinearity of the system of equations. As artificial viscosity stabilization needs the computation of modified stiffness matrices which includes the square root of the artificial viscosity function and because of the nonlinear characteristics of the Euler fluxes which need to be consistently integrated, one needs to evaluate the Lagrange basis functions off the theoretically optimal LGL quadrature points. This often subverts the most remarkable feature of the spectral nodal approach, namely, the indistinction between collocation and quadrature points. On the contrary, the modal formulation showed computationally insensitive for any nonlinearity calculation being very straightforward to cope with all consistent integration procedures. Results also made clear that although elementwise constant viscous function can stabilize the numerical solutions, it works at the expense of much artificial viscosity addition spread over the entire domain of the problem and therefore with no locality advantage as claimed in the original publication of Persson & Peraire (2006).

ACKNOWLEDGEMENTS

The authors would like to thank the IBM Research Brazil laboratory for the technical support and funding that enabled this work. They also extend their gratitude to the State University of Campinas and the Federal University of São Carlos for supporting this current collaborative research.

REFERENCES

Cockburn, B., Shu, C. W., 1998. The local discontinuous Galerkin method for time-dependent convection-diffusion systems. *SIAM Journal on Numerical Analysis*, 35, 2440-2463.

Hesthaven, J. S. and Warburton, T., 2008. *Nodal Discontinuous Galerkin Methods: Algorithms, Analysis, and Applications*. Springer-Verlag.

Karniadakis, G. E. and Sherwin, S. J., 2005. *Spectral/hp Element Methods for Computational Fluid Dynamics*, 2nd. ed., Oxford University Press.

Klöckner, A., Warburton, T. and Hesthaven, J. S., 2011. Viscous Shock Capturing in a Time-Explicit Discontinuous Galerkin Method, *Mathematical Modelling of Natural Phenomena*, vol. 6, n. 3, pp. 57-83.

Nogueira Jr., A. C., Almeida, J. L. S. and Silva, C. A. C., 2016. On the choice of shock capturing schemes for the solution of the LWR traffic flow equation using a high order modal discontinuous Galerkin discretization, *Proceedings of the ECCOMAS 2016: European Congress*

on Computational Methods in Applied Sciences and Engineering, Crete Island, Greece, June 05-10.

Nogueira Jr., A. C., Moore S., 2015. Solution of the LWR nonlinear traffic flow model using a discontinuous Galerkin FEM approach, *Proceeding of CILAMCE 2015: XXXVI Ibero-Latin American Congress on Computational Methods in Engineerring*, Rio de Janeiro, Brazil, November 22-25

Persson, P-O. and Peraire, J., 2006. Sub-Cell Shock Capturing for Discontinuous Galerkin Methods, *Proceedings of the 44th AIAA Aerospace Sciences Meeting and Exhibit*, volume 112.

Sod, G. A., 1978. A Survey of Several Finite Difference Methods for Systems of Nonlinear Hyperbolic Conservation Laws, *Journal of Computational Physics*, vol. 21, pp. 1-31.